Article

Origin of shear induced 'catching bonds' on half Heusler thermoelectric compounds XFeSb (X = Nb, Ta) and SnNiY (Y = Ti, Zr, Hf)

Check for updates

Haoqin Ma[1], Xiege Huang[1], Zhongtao Lu[1], Xiaobin Feng[1,2], Bo Duan[1,2], Wenjuan Li[1], Yinhan Liu[1], Pengcheng Zhai[1,2], Guodong Li [1,2] ✉ & Qingjie Zhang [1,2]

Half Heusler materials exhibit excellent thermoelectric and mechanical properties, rendering them potential candidates for advanced thermoelectric devices. Currently, the developments on interrelated devices are impeded by their inherent brittleness and limited ductility. Nevertheless, it exists the potential ductility on half Heusler materials with face-centered cubic sub-lattices through the expectation of the occurrence of shear-induced 'catching bonds' which can result in excellent ductility on other face-centered cubic materials. This work focuses on half Heusler thermoelectric materials XFeSb (X = Nb, Ta) and SnNiY (Y = Ti, Zr, Hf), the shear deformation failure processes are deeply investigated through the first principle calculations. Shear-induced 'catching bonds' are found on XFeSb (X = Nb, Ta) along the (111)/<-1-12> slip system, which releases the internal stress and exactly resulting in the potential ductility. According to the thermodynamic criterion based on generalized stacking fault energy, the essence of shear-induced 'catching bonds' are interpreted as the (111)/<-110> slips formed by several 1/3(111)/<-1-12> partial dislocations motions. During the (111)/<-1-12> shear on SnNiY (Y = Ti, Zr, Hf), the structural integrity is maintained without inducing 'catching bonds'. Different deformation processes occurring in the identical crystal structure are elucidated through the energy explanation, revealing that shear-induced 'catching bonds' originate from the crystal plane cleavage on the (111) plane. The present works offer significant advantages for the assessment and comprehension of shear-induced 'catching bonds' in other materials and facilitate the development of XFeSb (X = Nb, Ta)-based thermoelectric devices with excellent ductility.

After decades of advancements in thermoelectrics, the realization of stable and efficient thermoelectric devices appears to be on the horizon[1,2]. Currently, the developing progress of thermoelectric devices is hindered by their limited mechanical properties[3]. During applications, in order to prevent failure or fracture caused by external mechanical or thermal stress, it is crucial for thermoelectric devices to possess excellent thermodynamic stability and robust mechanical properties, in which the intrinsic mechanical properties of thermoelectric materials play a crucial role[4,5]. Furthermore, recent advancements in flexible thermoelectric materials have opened up possibilities for the development of wearable thermoelectric devices, necessitating the utilization of thermoelectric materials with exceptional ductility[6]. However, the majority of thermoelectric materials exhibit brittleness, low strength, low toughness, and low ductility. Therefore, searching for thermoelectric materials with excellent mechanical properties and conducting thorough investigations into the intrinsic mechanical properties of known thermoelectric materials holds immense practical significance for designing and developing enduringly stable thermoelectric devices.

[1]Hubei Key Laboratory of Theory and Application of Advanced Materials Mechanics, School of Science, Wuhan University of Technology, 430070 Wuhan, China. [2]State Key Laboratory of Advanced Technology for Materials Synthesis and Processing, Wuhan University of Technology, 430070 Wuhan, China. ✉e-mail: guodonglee@whut.edu.cn

Among the thermoelectric family, half Heusler compounds (HHCs) exhibit both excellent thermoelectric properties (ZT > 1 for both n- and p-type) and robust mechanical properties, resulting in the high expectation for developing advanced thermoelectric devices[7,8]. Numerous works[3] have been conducted on the mechanical properties of HHCs, revealing that their elastic moduli range from 144 to 236 GPa, fracture toughness range from 1.8 to 2.3 MPa m$^{1/2}$, and thermal expansion range from 8.8 to 11.2 × 10^{-6} K^{-1}. Our previous work has investigated the intrinsic mechanical properties of SnNiTi and revealed that it possesses the lowest ideal shear strength of 10.52 GPa along the (111)/<-110> slip systems with the softening Ti–Sn covalent framework during deformations[9]. Despite the high mechanical properties exhibited by HHCs within the thermoelectric family, their inherent brittleness and limited ductility have also been consistently reported[3,10], posing a significant challenge for the development of enduringly stable thermoelectric devices, particularly flexible ones.

To achieve excellent ductility on materials, previous works have revealed that the presence of shear-induced 'catching bonds' can be effective on face-centered cubic materials[11]. 'Catching bonds' refers to the structural rearrangement process during deformations, wherein partial bonds are cracked and simultaneously several bonds are formed, ultimately resulting in the restoration of crystal structure to the initial state. Further deformations can result in the repetitive deformation response as the initial state. Theoretic infinite repetitive deformation response can thereby result in excellent ductility. Our previous works have observed 'catching bonds' in nano-twinned InSb during the (111)/<−1-12> shear[11] while the distinguishing structural characteristic of nano-twinned InSb lies in its two interpenetrating face-centered cubic sub-lattices. It captivates our attention with the anticipation of the occurrence of shear-induced 'catching bonds' in HHCs crystallized by three interpenetrating face-centered cubic sub-lattices[3,12], which can result in potential ductility.

This work, focuses on half Heusler thermoelectric materials XFeSb (X = Nb, Ta) and SnNiY (Y = Ti, Zr, Hf), mechanical properties and the shear deformation processes are deeply investigated through the first principle calculations. Shear-induced 'catching bonds' are observed on XFeSb (X = Nb, Ta) along the (111)/<-1-12> slip system, which releases the internal stress without destroying structural integrity, exactly resulting in the theoretically infinite ductility. Through the generalized stacking fault energy-based thermodynamic criterion, 'catching bonds' are considered as the (111)/<−110> slips composed of several 1/3(111)/<-1-12> partial dislocation motions. The shear deformation processes along the (111)/<-1-12> slip system on SnNiY (Y = Ti, Zr, Hf) exhibit differences in that the structural integrity is consistently maintained without inducing 'catching bonds'. The different deformation mechanism within the identical crystal structure is explained by the energy criterion that shear-induced 'catching bonds' can only occur when the systematic energy during the shear processes reaches the cleavage energy threshold while simultaneously a reasonably stacking fault energy valley and a viable dislocation motion path exist. The present work is beneficial in assessing and comprehending shear-induced 'catching bonds' in other materials, and meanwhile facilitates the development of XFeSb (X = Nb, Ta)-based thermoelectric devices with excellent ductility.

Results and discussion
Crystal structure and elastic properties of XFeSb (X = Nb, Ta) and SnNiY (Y = Ti, Zr, Hf)

The optimized crystal structures of XFeSb (X = Nb, Ta) and SnNiY (Y = Ti, Zr, Hf) strictly conform to the standard crystal structure of HHCs with the space group of $F\bar{4}3m$ (No. 216), which is shown in Supplementary Fig. 2. With the chemical formula written in the order of ABC, A atoms occupy 4a sites at (0, 0, 0), B atoms occupy 4c sites at (0.25, 0.25, 0.25), C atoms occupy 4b sites at (0.5, 0.5, 0.5), while the remaining 4d sites at (0.75, 0.75, 0.75) are vacant. A, B, and C atoms jointly constitute three interpenetrated face-centered cubic sub-lattices. The calculated lattice parameters of XFeSb (X = Nb, Ta) and SnNiY (Y = Ti, Zr, Hf) are 5.96, 5.96, 5.94, 6.14, and 6.11 Å, respectively, as listed in Supplementary Table 1, which exhibit a high level of concordance with previous works[9,12–15].

The elastic properties of XFeSb (X = Nb, Ta) and SnNiY (Y = Ti, Zr, Hf) are also listed in Supplementary Table 1. Young's modulus of XFeSb (X = Nb, Ta) and SnNiY (Y = Ti, Zr, Hf) are 201.15, 215.64, 170.96, 183.96, and 198.84 GPa while their shear modulus are 77.54, 83.50, 67.27, 73.51, and 79.78 GPa, respectively. In terms of numerical value, they exhibit state-of-the-art performance when compared to other thermoelectric materials such as Bi_2Te_3 (Young's modulus of 61.6 GPa and shear modulus of 24.8 GPa)[16] and $CoSb_3$ (Young's modulus of 145.38 GPa and shear modulus of 59.45 GPa)[17].

Ideal shear strength and fracture toughness of XFeSb (X = Nb, Ta) and SnNiY (Y = Ti, Zr, Hf)

Along the typical (111)/<-1-12>, (111)/<11-2>, and (111)/<-110> slip systems on the face-centered cubic structure[18], the shear stress–strain response of XFeSb (X = Nb, Ta) and SnNiY (Y = Ti, Zr, Hf) are investigated and the results of the representative TaFeSb and SnNiTi are shown in Supplementary Fig. 3. Among all the slip systems, (111)/<-1-12> slip system exhibits the lowest ideal shear strength in both TaFeSb and SnNiTi, indicating that (111)/<-1-12> slip system should be easiest activated.

Focus on the (111)/<-1-12> slip system, the shear stress–strain response of XFeSb (X = Nb, Ta) and SnNiY (Y = Ti, Zr, Hf) are shown in Fig. 1 while the ideal shear strength and fracture toughness are shown in Table 1. Along the (111)/<-1-12> slip system, the ideal shear strength of XFeSb (X = Nb, Ta) and SnNiY (Y = Ti, Zr, Hf) is located at the order of 10^1 GPa. Since there is hardly direct shear strength data in the experiments, other strength is compared in this work. Compared with the experimental compression strength of 2.5–4.45 GPa on half Heusler materials $Hf_{0.44}Zr_{0.44}Ti_{0.12}CoSb_{0.8}Sn_{0.2}$ with different synthesis and testing methods[19], our theoretical shear strength is obviously higher, which is caused by the ideal perfect single crystal and ideal loading conditions used in the first principle calculations. The fracture toughness of SnNiY (Y = Ti, Zr, Hf) is located at the order of 100 MPa m$^{0.5}$ while the fracture toughness of XFeSb (X = Nb, Ta) is vacant due to the lack of the negative shear stress. The resistance to the shear deformation of XFeSb (X = Nb, Ta) and SnNiY (Y = Ti, Zr, Hf) surpasses most of the other thermoelectric materials, such as
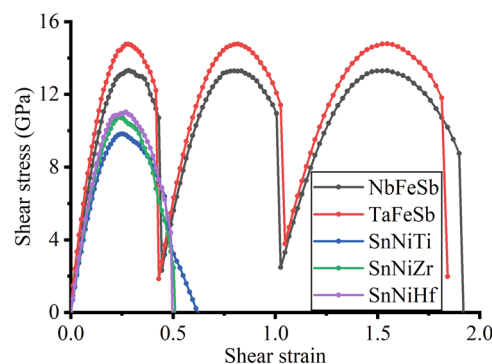

Fig. 1 | Shear stress-strain response of XFeSb (X = Nb, Ta) and SnNiY (Y = Ti, Zr, Hf) along the (111)/<−1-12> slip system.

Table 1 | Ideal shear strength and fracture toughness of XFeSb (X = Nb, Ta) and SnNiY (Y = Ti, Zr, Hf) along the (111)/<−1-12> slip system

Compounds	Ideal shear strength (GPa)	Fracture toughness (MPa m$^{0.5}$)
NbFeSb	13.32	/
TaFeSb	14.76	/
NiSnTi	9.81	1.01
NiSnZr	10.74	1.05
NiSnHf	11.03	1.12

CoSb$_3$ (7.21 GPa and 0.52 MPa m$^{0.5}$) and PbTe (3.45 GPa and 0.26 MPa m$^{0.5}$)[20], indicating that XFeSb (X = Nb, Ta) and SnNiY (Y = Ti, Zr, Hf) are potential to serve as mechanically robust thermoelectric materials.

As shown in Fig. 1, XFeSb (X = Nb, Ta) and SnNiY (Y = Ti, Zr, Hf) exhibit different shear stress–strain response along the (111)/<-1-12> slip system. The shear stress–strain response of XFeSb (X = Nb, Ta) exhibits repetitive stress-releasing processes that after each stress reduction process, the shear stress does not reach a negative value and further shear deformation can result in a repeat stress–strain response. The ideal shear strength of each stress–strain response remains consistent, indicating that each stress–strain response may be equivalent. Such stress–strain responses are similar to the characteristic features of 'catching bonds' stress–strain responses[11], which should be further verified by comprehensively investigating their deformation mechanism. As for SnNiY (Y = Ti, Zr, Hf), the shear stress–strain responses exhibit common behavior without drastic stress reduction processes until reaching the negative shear stress.

Shear-induced 'catching bonds' on XFeSb (X = Nb, Ta) along the (111)/<-1-12> slip system

Figure 2 shows the atomic configuration of TaFeSb during the (111)/<-1-12> shear combined with the dynamic response of the chemical bonds. From 0 to 0.42 strain, the crystal structure of TaFeSb undergoes uniform deformation to resist deformation. Ta6–Sb5 bond exhibits the greatest variation in bond length as shown in Fig. 2d, increasing from 3.00 to 3.90 Å (an increase of 30%), indicating that stretched Ta–Sb bonds dominate the deformation in this process. From 0.42 to 0.43 strain, all bonds across the (111) plane between Ta7 and Sb5 atoms are cracked and recombined while such particular (111) plane is marked as the purple line in Fig. 2c. The bond length variations of representative cracked Ta6–Fe3 bond marked as the orange dotted line in Fig. 2c and formed Fe3–Ta7 bond are shown in Fig. 3b. The bond length of Ta6–Fe3 bond and Fe3–Ta7 bond have been interchanged during the stress reduction process. By conducting a meticulous comparison between the atomic configuration of TaFeSb at 0.43 strain and 0 strain as shown in Fig. 3a, the deformed atomic configuration is superimposed onto the perfect TaFeSb supercell, indicating that the actual atomic configuration is entirely equivalent. The deformed atomic configuration into the initial state can effectively release the internal stress, which is consistent with previously reported 'catching bonds'[21]. Therefore, combined with the shear stress–strain response as shown in Fig. 1, herein, we believe that TaFeSb undergoes 'catching bonds' during the (111)/<-1-12> shear.

To verify the repeatability of 'catching bonds', Fig. 3 shows the atomic configurations of TaFeSb after each stress-releasing process combined with the dynamic response of the representative Ta6–Fe3 and Ta7–Fe3 bonds. It is observed that the atomic configuration and the corresponding bond lengths will invariably revert to the initial state without destroying structural integrity, indicating that 'catching bonds' can happen infinitely. The repeatability feature of 'catching bonds' can result in the theoretically infinite fracture strain, leading to theoretical infinite fracture toughness. Therefore, theoretically, TaFeSb can exhibit excellent ductility along the (111)/<-1-12> slip system, which is beneficial for developing flexible thermoelectric devices.

To further investigate the essence of 'catching bonds', a partially enlarged diagram is shown in Fig. 2c, indicating that 'catching bonds' result in the cracking of the Ta6–Fe3 bond and the formation of Fe3–Ta7 bond. Such a structural rearrangement process reminds us of the similar phenomenon reported previously on diamond[22] and metals[23], which is considered as the dislocation-induced slip[24]. Through such thought, 'catching bonds' can be indeed understood as (111)/<-110> slip marked as the purple arrow in the partially enlarged diagram of Fig. 2a. Intuitively, the observed (111)/<-110> slip can be attributed to the presence of the (111)/<-110> perfect dislocation, however, caution must be exercised in directly associating this slip with the (111)/<-110> perfect dislocation due to the absence of direct

observation of the intermediate process during structural mutation. The direct first principle simulations can only capture the atomic configuration before and after the structural mutation while the intermediate process solely aims to identify the energy-minimizing procedure but does not accurately depict the true atomic motion[22]. In order to elucidate the intermediate process on the (111)/<-110> slip, the thermodynamic criterion should be imposed through the generalized stacking fault energy (GSFE).

Figure 4a shows the schematic diagram of the calculation model for the GSFE calculations, which comprise three independent (111) planes including one shuffle plane (abbreviated as S plane hereafter) and two glide planes (abbreviated as G1 and G2 planes hereafter). The dislocation displacement-dependent GSFE results of TaFeSb along the typical (111)/<-1-12>, (111)/<-110> slip systems are shown in Fig. 4b. Partial data points on the G1 and G2 planes are absent due to the computational non-convergence resulting from the inadequate input atomic configuration with various overlapping atoms and these data points certainly exhibit higher GSFE than the convergence points. Among three independent (111) planes, the GSFE results on the S plane exhibit comparatively lowest value along both the (111)/<-1-12> and (111)/<-110> slip systems, indicating that the dislocation activation on the S plane is prior in TaFeSb. Herein, the S plane precisely aligns with the purple dotted line depicted in Fig. 2c, indicating the bond cracking is exactly what happened on the S plane.

In addition, on the S plane, TaFeSb exhibits the unstable stacking fault energy γ_{us} of 2.35 J m^{-2} along the (111)/<-110> slip system and 2.55 J m^{-2} along the (111)/<-1-12> slip system, while the stable stacking fault energy γ_s exists along the (111)/<-1-12> slip system with the value of 1.57 J m^{-2} at the dislocation displacement of $1/3 \times b$. Numerically, γ_s is significantly less than γ_{us}, indicating that just in terms of energy, $1/3(111)$/<-1-12> partial dislocation on the S plane is considered to be activated in TaFeSb.

Certainly, the (111) plane exhibits a multitude of orientations not merely including <-1-12> and <-110>, while the GSFE result along whole the S plane of TaFeSb is shown in Fig. 4c. It is found that an energy valley has existed at the dislocation displacement of equivalent (111)/<-110> perfect dislocation and a viable energy pathway to this energy valley can be identified through two $1/3(111)$/[-1-12] partial dislocation motions. Therefore, through the GSFE-based thermodynamic criterion, the (111)/<-110> slip observed during the (111)/<-1-12> shear of TaFeSb can be regarded as two $1/3(111)$/<-1-12> partial dislocations motions instead of the (111)/<-110> perfect dislocation. The manifestation of such dislocation-induced slip in the atomic configuration is shown in the enlarged diagram of Fig. 2a that (111)/<-110> slip marked as purple arrow can be decomposed into two $1/3(111)$/<-1-12> partial dislocations motions marked as black arrows. In summary, the essence of 'catching bonds' is regarded as the continuous $1/3(111)$/<-1-12> partial dislocations motions.

The shear performance of NbFeSb along the (111)/<-1-12> slip systems is similar to that of TaFeSb with shear-induced 'catching bonds', which are shown in Supplementary Fig. 4.

Deformation failure mechanism of SnNiY (Y = Ti, Zr, Hf) along the (111)/<-1-12> slip system

Figure 5 show the atomic configurations of SnNiTi during the (111)/<-1-12> shear, accompanied by the dynamic response of chemical bonds. Different from the shear-induced 'catching bonds' observed on XFeSb (X = Nb, Ta), within the entire shear strain range, the crystal structure of SnNiTi undergoes almost uniform deformation to resist deformation without obvious bond cracking. Sn6–Ti5 bond exhibits continuous increase with the greatest variation in bond length, indicating that stretched Sn–Ti bonds dominate the deformation. Except Sn6–Ti5 bond, the bond length of the other bonds is almost unchanged. The structural integrity is always maintained while 'catching bonds' are not observed. The internal stress is gradually released through softening the crystal structure.

The shear performance of SnNiZr and SnNiHf along the (111)/<-1-12> slip systems are similar to that of SnNiTi without inserting 'catching bonds', which are shown in Supplementary Figs. 5 and 6.

Fig. 2 | The atomic configurations and dynamic chemical bonds length of TaFeSb before first stress releasing process during the (111)/<–1-12> shear. **a–c** The atomic configuration of TaFeSb projected onto the (–110) and (111) planes during the (111)/<–1-12> shear at the original shear strain of 0, shear strain before stress releasing of 0.42, and shear strain after stress releasing of 0.43, respectively. The partial structure are enlarged. **d** The dynamic response of all non-equivalent chemical bonds before first stress releasing process.
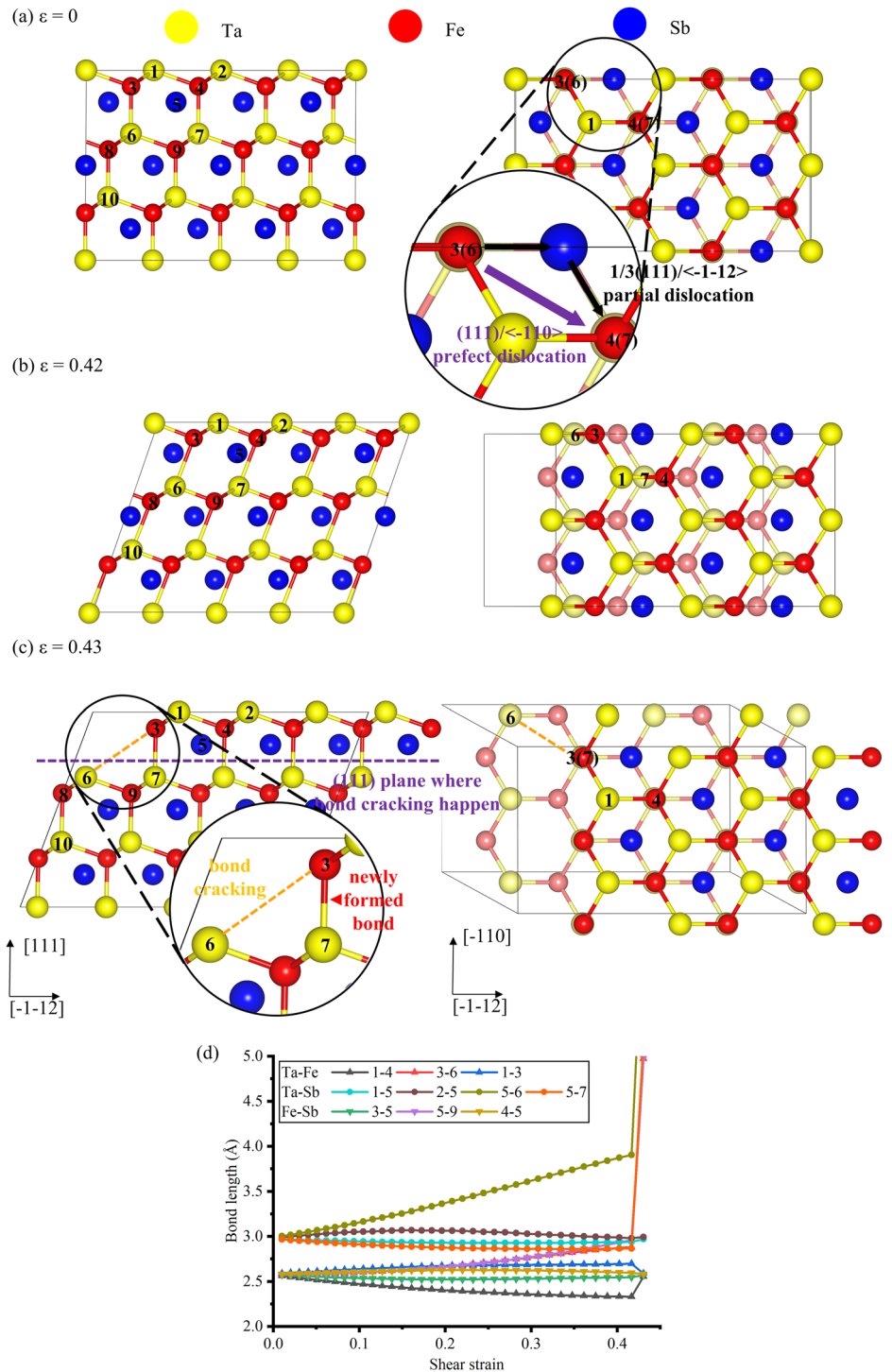
Energy explanation on the origin of shear-induced 'catching bonds'

XFeSb (X = Nb, Ta) and SnNiY (Y = Ti, Zr, Hf), with identical face-centered cubic sub-lattices, exhibit different shear responses along the (111)/<–1-12> slip system. The former is characterized by the presence of 'catching bonds' while the latter lacks such a feature, rendering it high significance for investigating the origin of 'catching bonds'. As shown in Fig. 2 and S4, shear-induced 'catching bonds' observed in XFeSb (X = Nb, Ta) can be considered as occurring through a two-step process. The first step involves bonds cracking on the S plane resulting in the crystal plane cleavage while the second step is the re-bonded process. In SnNiY (Y = Ti, Zr, Hf), the first step

of crystal plane cleavage does not happen, thus avoiding the second step and completing 'catching bonds'. Therefore herein, we guess that the precondition of the 'catching bonds' should be the occurrence of the crystal plane cleavage during the shear processes.

To access the occurrence of the crystal plane cleavage, the thermodynamic criterion can be employed by applying a threshold based on the cleavage energy γ_c. When the systematic energy during the shear processes exceeds the cleavage energy threshold, the crystal plane cleavage occurs, otherwise, the structural integrity is maintained. Figure 6 shows the shear strain-dependent relative systematic energy of XFeSb (X = Nb, Ta) and SnNiY (Y = Ti, Zr, Hf) during the

Fig. 3 | the atomic configurations and dynamic chemical bonds length of TaFeSb after each stress releasing process during the (111)/<−1-12> shear. **a** The atomic configurations of TaFeSb after each stress releasing process at shear strains of 0.43, 1.05, and 1.84, respectively. The shadow background is prefect TaFeSb supercell. **b** The dynamic response of Ta6-Fe3 and Ta7-Fe3 bonds through three stress releasing processes.
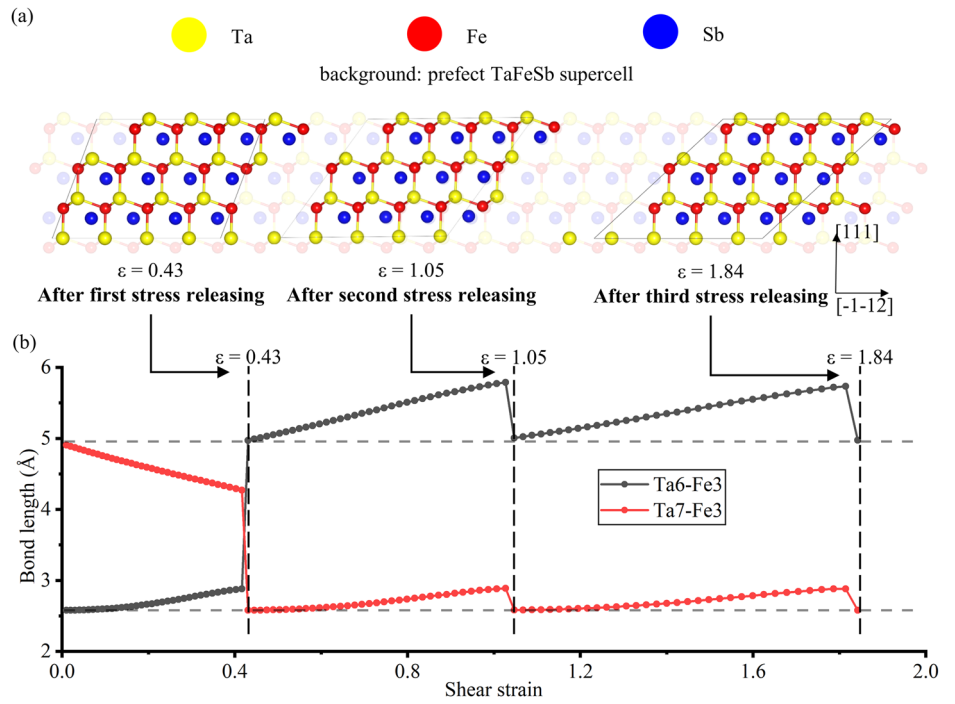

Fig. 4 | The generalized stacking fault energy calculations model and generalized stacking fault energy results of TaFeSb. a The schematic diagram of the calculation model for the GSFE calculations including three independent (111) planes. **b** Dislocation displacement dependent GSFE of TaFeSb along the (111)/<−110> and (111)/<−1-12> slip systems. **c** GSFE of TaFeSb on whole the S plane. The x- and y-axis are along the [−1-12] and [−110] orientations, respectively, containing the complete burgers vector. The color legend exhibits a logarithmic distribution.
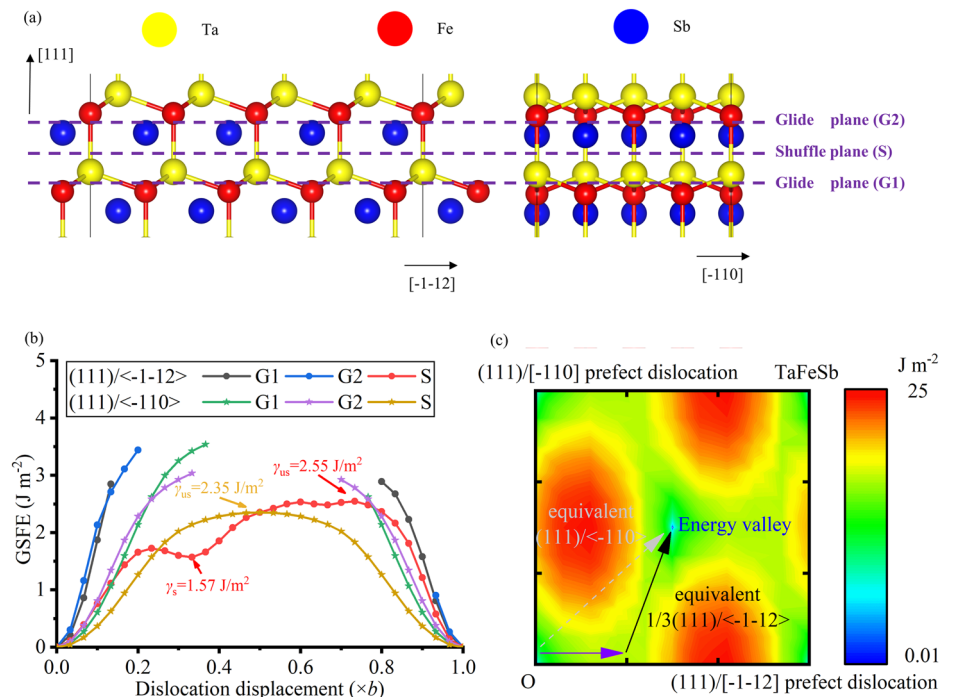
(111)/<-1-12> shear, accompanied by the corresponding cleavage energy threshold on the S plane. The relative systematic energy is aligned to the systematic energy at 0 strain. During the shear process, the systematic energy of XFeSb (X = Nb, Ta) gradually increases and finally reaches the cleavage energy threshold, resulting in the crystal plane cleavage. In contrast, the systematic energy of SnNiY (Y = Ti, Zr, Hf) gradually increases and reaches a yield value of 3.16, 3.25, and 3.35 J m^{-2}, respectively, which are lower than the cleavage energy threshold of 3.59, 3.64, 3.77 J m^{-2}, respectively, resulting in the maintenance of the structure integrity without crystal plane cleavage. The results from the thermodynamic criterion verify our guess and meanwhile agree well with our shear simulation mentioned above.

The above discussion in the section "Generalize stacking fault energy calculations" has highlighted that the essence of 'catching bonds' is the dislocation-induced slip. Combined with the origin of 'catching bonds' found through the energy criterion as the crystal plane cleavage, shear-induced 'catching bonds' are ultimately regarded as the crystal plane cleavage followed by dislocation motions. It is worth noting here that the understanding of shear-induced 'catching bonds' extends beyond the face-centered cubic crystal structure, suggesting the potential for identifying ductility in other materials. Shear-induced 'catching bonds' only require that the systematic energy during shear processes reaches the cleavage energy threshold, while simultaneously ensuring a reasonably stacking fault energy valley and a viable dislocation motion path.

Fig. 5 | The atomic configurations and dynamic chemical bonds length of SnNiTi before first stress releasing process during the (111)/<–1-12> shear. a–d The atomic configuration of SnNiTi projected onto the (–110) planeduring the (111)/<–1-12> shear, at original shear strains of 0, three shear strains after the peak stress of 0.46, 0.49, and 0.61, respectively. **e** The dynamic response of all non-equivalent chemical bonds.
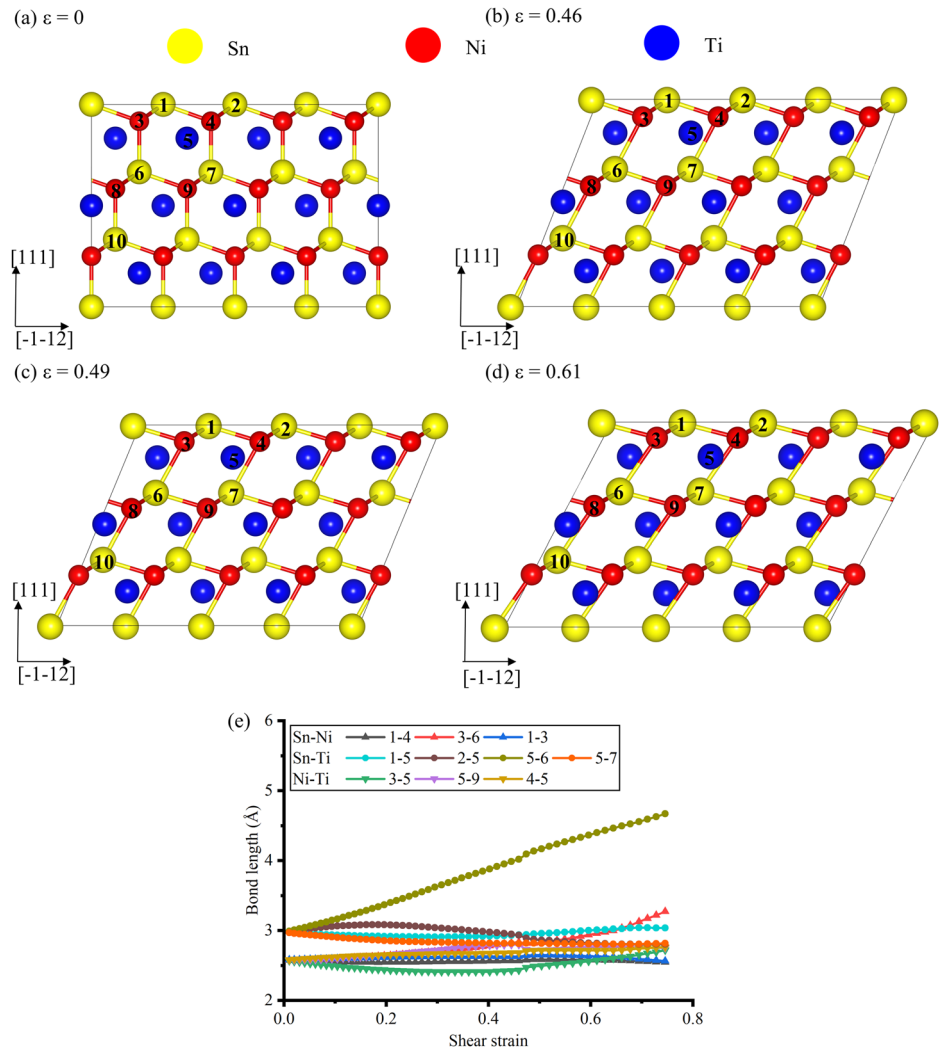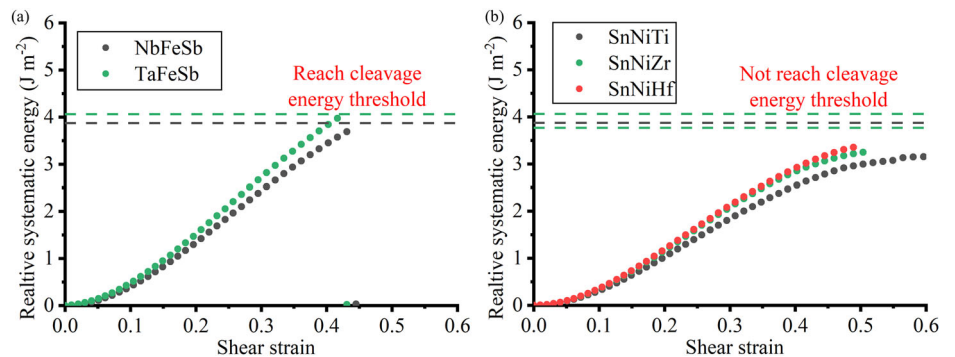

Fig. 6 | Shear strain dependent relative systematic energy of XFeSb (X = Nb, Ta) and SnNiY (Y = Ti, Zr, Hf) during the (111)/<–1-12> shear. a and **b** Shear strain dependent relative systematic energy of XFeSb (X = Nb, Ta) and SnNiY (Y = Ti, Zr, Hf) during the (111)/<–1-12> shear. Dotted lines are the cleavage energy threshold on the S plane.

In summary, the shear-induced 'catching bonds' are investigated on half Heusler thermoelectric materials XFeSb (X = Nb, Ta) and SnNiY (Y = Ti, Zr, Hf). Shear-induced 'catching bonds' are found along the (111)/<-1-12> slip system on XFeSb (X = Nb, Ta), resulting in theoretical infinite fracture toughness. Through the generalized stacking fault energy-based thermodynamic criterion, 'catching bonds' are interpreted as the (111)/<-110> slips composed of several 1/3(111)/<-1-12> partial dislocations. The shear deformation process along the (111)/<-1-12> slip system on SnNiY (Y = Ti, Zr, Hf) shows a difference that the structural integrity is consistently maintained without the occurrence of 'catching bonds'. Through the energy explanation, shear-induced 'catching bonds' are regarded as the crystal plane cleavage followed by dislocation motions while

the precondition necessitates that the systematic energy during the shear deformations reaches the cleavage energy threshold and simultaneously ensures the presence of a reasonably stable stacking fault energy and a viable dislocation motion path. A deep understanding of the shear-induced 'catching bonds' can be beneficial in the assessment and comprehension of similar phenomena in other materials.

Methods
DFT calculation settings
The first principle calculations were completed through density functional theory (DFT) based Vienna ab initio Simulation Package (VASP)[25] with Perdew–Burke–Ernzerhof (PBE) exchange-correlation functional and

projector-augmented wave (PAW) method[26]. The structural convergence criterion was set with plane wave cutoff energy of 600 eV, Gamma-centered k-points reciprocal space sampling of $7 \times 7 \times 7$, energy difference for solving the electronic wave function of 1×10^{-7} eV, and force difference for geometry optimization of 1×10^{-2} eV Å^{-1}.

Mechanical properties calculations

The elastic constants were calculated directly through the built-in program on VASP. From the calculated elastic constants, bulk modulus, shear modulus, Young's Modulus, and Poisson's ratio were obtained through the Voigt–Reuss–Hill method[27], while hardness was obtained by the empirical equation[28]. The calculation models for structural relaxation and elastic constants on the unit cells include 12 atoms.

The shear simulations were realized by imposing the shear strain on a particular slip system while the five other strain components were allowed to be relaxed[11,17,20,29–34]. The calculation models for the shear simulations are employed on the supercell including 96, 48, 72, 72, and 72 atoms along the (001)/<100>, (001)/<110>, (111)/<-110>, (111)/<-1-12>, and (111)/<11-2> slip systems, respectively. The variation in the atomic numbers is attributed to the different structural modeling in different slip systems. The ideal shear strength was defined as the maximum shear stress during the shear process. Herein, the calculated mechanical strength corresponds to the theoretical maximum strength achievable in the experiments due to the ideal perfect crystal structure and the ideal loading conditions.

Only one kind of facture toughness K_{IIc} is considered in this work because the actual pure shear simulations can only match the sliding model while the estimation of the facture toughness K_{Ic} and K_{IIIc} should be achieved through other kinds of simulations. The fracture toughness K_{IIc} during the shear deformations can be expressed by Eq. (1) as[20,30]

$$K_{IIc}^2 = \frac{2G_{IIc}G}{1-\nu} = \frac{2G}{1-\nu} \int_0^{fracture} \sigma \, \mathrm{d}l \qquad (1)$$

where G was the shear modulus, ν was the Poisson's ratio, G_{IIc} was called the energy release rate while σ was the shear stress, l was the lattice displacement converted from the shear strain, and the upper limit of integral, fracture, corresponded to the shear strain where the shear stress reaching the negative value. The converted shear stress-lattice displacement curve of SnNiTi as an example was shown in Supplementary Fig. 1.

Generalize stacking fault energy calculations

The generalized stacking fault energy (GSFE) was calculated by the energy difference between the perfect structure and the structure with the inserted dislocations while atoms were only relaxed perpendicular to the slip plane[21]. The cleavage energy was calculated by the energy difference between the perfect crystal structure and the split crystal structure along the particular plane while atoms were unrelaxed. The calculation models used for generalized stacking fault energy calculations include 144 atoms with a 10 Å vacuum layer whose schematic diagrams are shown in Fig. 4a.

Data availability

The authors declare that the data supporting the findings of this study are available within the paper and its supplementary information files.

References

1. Cao, T. et al. Advances in the design and assembly of flexible thermoelectric device. *Prog. Mater. Sci.* **131**, 443–452 (2023).
2. Yang, Y. et al. Thermoelastic stress analysis of multilayered films in a micro-thermoelectric cooling device. *Acta Mech. Sin.* **28**, 1644–1650 (2012).
3. Rogl, G. et al. Mechanical properties of half-Heusler alloys. *Acta Mater.* **107**, 178–195 (2016).
4. Rogl, G. & Rogl, P. How Severe plastic deformation changes the mechanical properties of thermoelectric skutterudites and half Heusler alloys. *Front. Mater* **7**, 600261 (2020).
5. Tang, X. et al. A comprehensive review on Bi_2Te_3-based thin films: thermoelectrics and beyond. *Interdiscip. Mater.* **1**, 88–115 (2022).
6. Wang, H. et al. Synergetic enhancement of strength–ductility and thermoelectric properties of Ag_2Te by domain boundaries. *Adv. Mater.* **35**, 2302969 (2023).
7. Yu, J. et al. High performance p-type half-Heusler thermoelectric materials. *J. Phys. D. Appl. Phys.* **51**, 113001 (2018).
8. Yu, J. et al. Half-Heusler thermoelectric module with high conversion efficiency and high power density. *Adv. Energy Mater.* **10**, 2000888 (2020).
9. Li, G. et al. Enhanced ideal strength of thermoelectric half-Heusler TiNiSn by sub-structure engineering. *J. Mater. Chem. A* **4**, 14625–14636 (2016).
10. Casper, F. et al. Half-Heusler compounds: novel materials for energy and spintronic applications. *Semicond. Sci. Tech.* **27**, 063001 (2012).
11. Li, G. et al. Enhanced strength through nanotwinning in the thermoelectric semiconductor InSb. *Phys. Rev. Lett.* **119**, 215503 (2017).
12. Hobbis, D. et al. Structural, chemical, electrical, and thermal properties of n-type NbFeSb. *Inorg. Chem.* **58**, 1826–1833 (2019).
13. Çoban, C. et al. First principles study of the structural, mechanical, phonon, optical, and thermodynamic properties of half-Heusler (HH) compound NbFeSb. *Phys. Scr.* **90**, 095701 (2015).
14. Tian, Y. et al. Half-heusler thermoelectric materials: NMR. *Stud., J. Appl. Phys.* **128**, 055106 (2020).
15. Grytsiv, A. et al. Thermoelectric half-Heusler compounds TaFeSb and $Ta_{1-x}Ti_xFeSb$ ($0 \le x \le 0.11$): formation and physical properties. *Intermetallics* **111**, 106468 (2019).
16. Koc, H. et al. Structual, elastic, and electronic properties of opological insulators: Sb_2Te_3 and Bi_2Te_3. In *IEEE International Symposium on Applications of Ferroelectrics and Workshop on the Piezoresponse Force Microscopy* (ISAF/PFM) (2013).
17. Li, G. et al. Brittle failure mechanism in thermoelectric skutterudite $CoSb_3$. *Chem. Mater.* **27**, 6329–6336 (2015).
18. Zimmerman, J. A. et al. Generalized stacking fault energies for embedded atom FCC metals. *Model. Simul. Mater. Sci. Eng.* **8**, 103–115 (2000).
19. Aumand, M. et al. Multi-scale study of the deformation mechanisms of thermoelectric p-type half-Heusler $Hf_{0.44}Zr_{0.44}Ti_{0.12}CoSb_{0.8}Sn_{0.2}$. *J. Appl. Phys.* **124**, 175104 (2018).
20. Li, G. et al. Fracture toughness of thermoelectric materials. *Mater. Sci. Eng. R* **144**, 100607 (2021).
21. Wu, X. et al. Generalized-stacking-fault energy and surface properties for HCP metals: a first-principles study. *Appl. Surf. Sci.* **256**, 3409–3412 (2010).
22. Miyata, M. & Fujiwara, T. Ab initio calculation of peierls stress in silicon. *Phys. Rev. B* **63**, 045206 (2001).
23. Li, X. et al. Dislocation nucleation governed softening and maximum strength in nano-twinned metals. *Nature* **464**, 877–880 (2010).
24. Shi, X. et al. Room-temperature ductile inorganic semiconductor. *Nat. mater.* **17**, 421–426 (2018).
25. Kreese, G. & Fürthmuller, J. Efficient iterative schemes for ab initio total-energy calculations using a plane-wave basis set. *Phys. Rev. B* **54**, 11169–11186 (1996).
26. Blochl, P. E. Projector augmented-wave method. *Phys. Rev. B Condens. Matter* **50**, 17953–17979 (1994).
27. Wu, Z. et al. Crystal structures and elastic properties of superhard IrN_2 and IrN_3 from first principles. *Phys. Rev. B* **76**, 054115 (2007).

28. Chen, X. et al. Modeling hardness of polycrystalline materials and bulk metallic glasses. *Intermetallics* **19**, 1275–1281 (2011).
29. Li, G. et al. Mechanical softening of thermoelectric semiconductor Mg_2Si from nanotwinning. *Scr. Mater.* **157**, 90–94 (2018).
30. Li, G. et al. Micro- and macromechanical properties of thermoelectric lead chalcogenides. *ACS Appl. Mater. Int.* **9**, 40488–40496 (2017).
31. Li, G. et al. Superstrengthening Bi_2Te_3 through nanotwinning. *Phys. Rev. Lett.* **119**, 085501 (2017).
32. Li, G. et al. Deformation mechanisms in high-efficiency thermoelectric layered Zintl compounds. *J. Mater. Chem. A* **5**, 9050–9059 (2017).
33. Li, G. et al. Determining ideal strength and failure mechanism of thermoelectric $CuInTe_2$ through quantum mechanics. *J. Mater. Chem. A* **6**, 11743–11750 (2018).
34. Li, G. et al. Ideal strength and deformation mechanism in high-efficiency thermoelectric SnSe. *Chem. Mater.* **29**, 2382–2389 (2017).

Author contributions
H.M. dominant the whole first principle calculations, the result processing and analysis, and was a major contributor in writing the manuscript. X.H. provided the reliable computing equipment and participated in the calculation design and results analysis. Z.L. participated in the calculation design and results analysis. X.F. participated in the calculation design and results analysis. B.D. provided the foundation. W.L. participated in results analysis. Y.L. participated in results analysis. P.Z. participated in the results analysis and provided the foundation. G.L. provided the reliable computing equipment, participated in the calculation design and results analysis, and was a contributor in writing the manuscript. Q.Z. participated in results analysis and provided the foundation. All authors read and approved the final manuscript.

Competing interests
The authors declare no competing interests.

Additional information
Supplementary information The online version contains supplementary material available at https://doi.org/10.1038/s41524-024-01238-1.

Correspondence and requests for materials should be addressed to Guodong Li.

Reprints and permissions information is available at http://www.nature.com/reprints

Publisher's note Springer Nature remains neutral with regard to jurisdictional claims in published maps and institutional affiliations.